

See discussions, stats, and author profiles for this publication at: <https://www.researchgate.net/publication/228670224>

Utilising Minkowski Functionals for Image Analysis: a marching square algorithm

Article in *Journal of Statistical Mechanics Theory and Experiment* · December 2008

DOI: 10.1088/1742-5468/2008/12/P12015

CITATIONS

51

READS

252

3 authors, including:



Hubert Mantz
Hochschule Ulm

42 PUBLICATIONS 1,063 CITATIONS

[SEE PROFILE](#)



Karin Jacobs
Universität des Saarlandes

149 PUBLICATIONS 4,154 CITATIONS

[SEE PROFILE](#)

Some of the authors of this publication are also working on these related projects:



Effect of molecular weight distribution on polymers slip on solid substrates [View project](#)

Utilizing Minkowski functionals for image analysis: a marching square algorithm

Hubert Mantz¹, Karin Jacobs¹ and Klaus Mecke²

¹ Universität des Saarlandes, Experimentalphysik, D-66041 Saarbrücken, Germany

² Institut für Theoretische Physik, Universität Erlangen-Nürnberg, Staudtstrasse 7, D-91058 Erlangen, Germany

E-mail: h.mantz@physik.uni-saarland.de, k.jacobs@physik.uni-saarland.de and klaus.mecke@physik.uni-erlangen.de

Received 15 May 2008

Accepted 24 November 2008

Published 22 December 2008

Online at stacks.iop.org/JSTAT/2008/P12015

[doi:10.1088/1742-5468/2008/12/P12015](https://doi.org/10.1088/1742-5468/2008/12/P12015)

Abstract. Comparing noisy experimental image data with statistical models requires a quantitative analysis of grey-scale images beyond mean values and two-point correlations. A real-space image analysis technique is introduced for digitized grey-scale images, based on Minkowski functionals of thresholded patterns. A novel feature of this marching square algorithm is the use of weighted side lengths for pixels, so that boundary lengths are captured accurately. As examples to illustrate the technique we study surface topologies emerging during the dewetting process of thin films and analyse spinodal decomposition as well as turbulent patterns in chemical reaction–diffusion systems. The grey-scale value corresponds to the height of the film or to the concentration of chemicals, respectively. Comparison with analytic calculations in stochastic geometry models reveals a remarkable agreement of the examples with a Gaussian random field. Thus, a statistical test for non-Gaussian features in experimental data becomes possible with this image analysis technique—even for small image sizes. Implementations of the software used for the analysis are offered for download.

Keywords: patterns, liquid films (experiment), pattern formation (theory), pattern formation (experiment)

Contents

1. Introduction: complex spatial patterns	2
2. Morphological measures for grey-scale images	5
2.1. Minkowski functionals	5
2.2. Grey-scale images	6
2.3. Discretized Minkowski functionals	8
3. Marching cube/marching square algorithm for grey-scale images	11
3.1. Marching square algorithm for Minkowski functionals	12
3.2. Implementation	15
4. Stochastic geometry: models for random spatial structures	16
4.1. Random lattice model	17
4.2. Gaussian random field model	18
4.3. Maximum cone field model	20
5. Applications: pattern analysis with Minkowski functionals	21
5.1. Pattern analysis of spinodal decomposition structures	22
5.2. Pattern analysis of chemical reaction–diffusion images	22
5.3. Pattern analysis of dewetting morphologies in thin liquid films	26
6. Conclusion	27
References	28

1. Introduction: complex spatial patterns

With the development of powerful imaging techniques such as scanning force microscopy (SPM), confocal microscopy and computer tomography, the analysis of spatial structures becomes more and more important in contemporary science. Irregular spatio-temporal patterns occur in many systems, including chemical reaction–diffusion systems, hydrodynamic convection or dewetting processes. Examples are given in figures 1 and 2. The rapid development of real-space imaging methods calls for a progression in scientific image analysis methods. Whilst the human eye can, in a qualitative manner, easily decide about similarity, mathematical descriptors for structures that are not perfectly symmetrical are not trivial. There is no straightforward and explicit measure for shapes which involve asymmetry and disorder.

Many statistical methods have been developed for the analysis of two- and three-dimensional patterns, their power and potential has been explored, and there are many successful applications, in particular in biometry, physics and medicine (for reviews, see [2]–[6]). Many scientists consider second-order characteristics such as the pair correlation function as particularly powerful and prefer to use variances to measure roughness, for instance. Whereas for regular patterns these measures provide useful information about characteristic length scales and orientational order, they are incapable of distinguishing irregular structures of different topology. It can be shown that

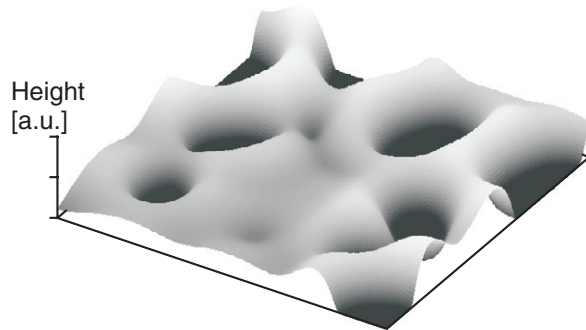


Figure 1. An example of the topographies to be analyzed: an image, gained by finite element simulation, of the dewetting process of a thin liquid film. The image carries height information in the grey-scale value $\hat{\rho}(\vec{x})$ (dataset taken from [1]). An animation explaining the principle of data analysis can be found as supporting material on the [webpage](#).

commonly used analysis methods like pair correlation functions and Fourier transforms are inapplicable for describing spatial features in quite a number of complex systems [5, 7]. They can only measure a distribution of distances; other morphological peculiarities remain undetected. Hence, extended topological measures have to be considered in these cases.

It is the aim of this paper to present a modern image analysis technique for digitized grey-scale images, based on the Minkowski functionals M_ν defined in integral geometry. A convenient mathematical tool to describe spatial configurations are intensity functions $\hat{\rho}(\vec{x}) \in \mathbb{R}$ which assign a grey value to each point $\vec{x} \in \mathbb{R}^2$ in the two-dimensional Euclidean plane. Such grey-scale patterns occur quite often in physics, for instance, as images of capillary waves at fluid interfaces, as varying thicknesses of thin block copolymer films on a solid substrate or as order parameters in Euclidean field theories. Since the very first x-ray scattering experiments, Fourier transformations of $\hat{\rho}(\vec{x})$ were used to identify order in spatial structures and were almost a synonym for structural analysis in statistical physics. However, in many cases ordered patterns are not the main feature in an image. For these images other tools have to be developed.

Usually, the interesting cases are those where $\hat{\rho}(\vec{x})$ exhibits a complex spatial structure, for instance, under demixing, dewetting or phase separation. An example is given in figure 1, showing the simulated topography of a thin liquid film that beads off a solid substrate. Patterns emerging from these finite element simulations have to be compared with corresponding structures from SPM measurements [1]. The images used in this study carry height information in the grey-scale value of each pixel $\hat{\rho}(\vec{x})$: a bright shade marks a high structure, while dark pixels describe the lower parts (details are given in section 5.2 below). In the spinodal decomposition shown in figure 2(a) the grey-scale $\hat{\rho}(\vec{x})$ denotes the concentration of fluorescent colloidal particles. A turbulent chemical pattern is shown in figure 2(b), where the grey-scale value $\hat{\rho}(\vec{x})$ of the image corresponds to the detected concentration of iodide I_3^- . For details about these systems, see sections 5.1–5.3, respectively.

Statistical methods that are sensitive to the morphology *or* shape of structures (curvatures and connectivity) have been investigated extensively in other fields such

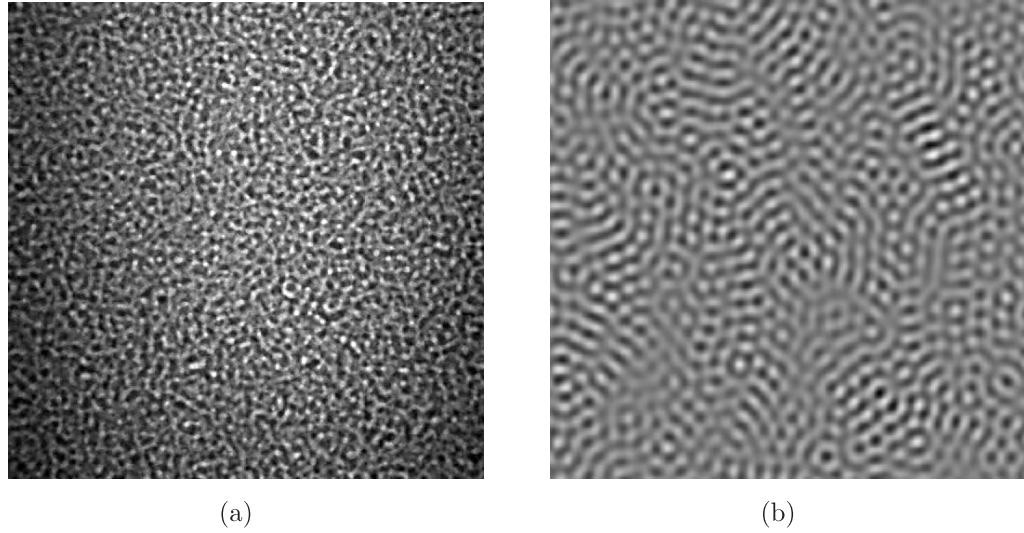


Figure 2. (a) Confocal scanning laser microscopy image of a phase-separating colloid-polymer mixture [8, 9]; courtesy Aarts and Lekkerkerker. A spinodal decomposition structure can be observed, which coarsens in time (see figure 11). (b) A turbulent pattern in a chemical reaction-diffusion system (figure from [10]). The grey-scale of the image corresponds to the concentration of iodide I_3^- .

as image analysis and pattern recognition [3], [11]–[13]. Here, we focus on Minkowski functionals $M_\nu(A)$ with $\nu = 0, 1, 2$ to characterize both the morphology *and* shape of domains A in two-dimensional Euclidean space. Such domains are obtained from grey-scale images by thresholding, so that the functionals are actually functions $M_\nu(\rho)$ of the grey-scale ρ (see section 2.2). Minkowski functionals have already been applied on various systems, for instance, on cosmological structures [24, 20, 21], on porous media [7], [25]–[27], as a tool for characterizing mesophases in block copolymer systems [28], for fractal analysis of alkane monolayer domains at SiO_2/air interfaces [15, 29] or for the biometry of tree stands in forests [30].

Here, we will focus on applications of Minkowski functionals as tools to analyze pattern formation in liquids, where grey-scale images can be measured which show features of Gaussian random fields. Examples comprise the identification of a linear dynamics regime in spinodal decomposition (section 5.1; [8, 9]), the identification of pattern transitions in two-dimensional chemical reaction-diffusion images (section 5.2; [10]), as well as the characterization of the dynamics in two-dimensional thin polymer films during dewetting processes (section 5.3; [1]). The analysis principles will be explained in more detail later in this text. In addition, implementations of the software used for the analysis are offered for download.

Although mean values of Minkowski functionals M_ν can often be calculated analytically for a wide range of stochastic models for grey-scale images such as the Gaussian random field model (see section 4.2), higher-order moments such as variances are difficult to calculate explicitly. Numerical algorithms as the one presented here are necessary to gain insight into the geometry of such stochastic patterns shown in figures 1 and 2, for instance. Furthermore, Minkowski functionals characterize spatial features of random fields which can be used to discriminate between different models and to test, for

example, for Gaussian random field behaviour in experimental data. Therefore, one needs a reliable algorithm to calculate these functionals numerically.

2. Morphological measures for grey-scale images

Almost every experimentally measured image can be considered as a union $A = \bigcup_{i=1}^N K_i$ of compact and convex subsets K_i in the two-dimensional Euclidean space \mathbb{R}^2 . This restriction to convex composed domains is, in particular, reasonable for digital image processing as one can consider a pixel as a compact and convex set. On this basis, functionals can be defined that describe the morphology of the structure, i.e. in our case of the image composed as a finite union of pixels. Integral geometry furnishes a suitable family of such morphological descriptors [14, 15], known as Minkowski functionals, that describe not only the content (area) but also topology (connectivity in our case) and shape (geometric curvatures) of the pattern.

2.1. Minkowski functionals

In d -dimensional space \mathbb{R}^d , there exist $d + 1$ Minkowski functionals M_0, \dots, M_d that describe a compact domain A . They can be defined by integrals of curvatures using differential geometry of smooth surfaces [5, 6]. If ∂A is the regular boundary of A and R_i are the principal radii of curvature for $i = 1, \dots, d - 1$, the functionals can be defined for $\nu \geq 1$ by

$$M_\nu(A) := \frac{\omega_{d-\nu}(\nu-1)!(d-\nu)!}{\omega_\nu \omega_d d!} \int_{\partial A} \sum_{\{i_1, \dots, i_{\nu-1}\}} \frac{1}{R_{i_1} \cdot \dots \cdot R_{i_{\nu-1}}} dS \quad (1)$$

with the volume $\omega_d = \pi^{d/2}/\Gamma(1 + d/2)$ of the d -dimensional unit ball [10]. The sum in equation (1) runs over all permutations i_ν containing ν of the $d - 1$ curvatures. By this definition, one obtains $\omega_0 = 1$, $\omega_1 = 2$, $\omega_2 = \pi$ and $\omega_3 = 4\pi/3$ and, in particular, in two dimensions the functionals

$$M_0(A) = \int_A d^2 \vec{r}, \quad M_1(A) = \frac{1}{2\pi} \int_{\partial A} d\vec{r}, \quad M_2(A) = \frac{1}{2\pi^2} \int_{\partial A} \frac{1}{R} d\vec{r} \quad (2)$$

with the Lebesgue measure $d^\nu \vec{r}$ of the ν -dimensional Euclidean space.

The fundamental importance of these functionals can be understood better if one considers Hadwiger's theorem, which proves the completeness of the Minkowski functionals [16]. It states that each additive, motion-invariant and continuous functional $\mathcal{F}(A)$ on sets $A \subset \mathbb{R}^d$ with $A \in \mathcal{R}$ can be expressed as a linear combination of $d + 1$ Minkowski functionals M_ν :

$$\mathcal{F}(A) = \sum_{\nu=0}^d f_\nu M_\nu(A). \quad (3)$$

The coefficients $f_\nu \in \mathbb{R}$ are determined independently of A . The theorem states that only the functionals defined by equation (3) have all of the following properties ($A, B, A_n \in \mathcal{R}$).

- Additivity: the functional of the union of two domains $A \cup B$ can be written as

$$\mathcal{F}(A \cup B) = \mathcal{F}(A) + \mathcal{F}(B) - \mathcal{F}(A \cap B). \quad (4)$$

Table 1. Minkowski functionals M_ν can be related to simple geometric quantities in two and three dimensions.

	ν	Geometric quantity	Minkowski functional M_ν
$d = 2$:	0	covered area F	$M_0(K) = F(K)$
	1	boundary length U	$M_1(K) = (1/2\pi)U(K)$
	2	Euler characteristic χ	$M_2(K) = (1/\pi)\chi(K)$
$d = 3$:	0	volume V	$M_0(K) = V(K)$
	1	surface S	$M_1(K) = \frac{1}{8}S(K)$
	2	mean curvature H	$M_2(K) = (1/2\pi^2)H(K)$
	3	Euler characteristic χ	$M_3(K) = (3/4\pi)\chi(K)$

- Motion invariance: the morphological functional of a set A is independent of its position and orientation in space. If \mathcal{G} is the group consisting of translational and rotational motions, then

$$\mathcal{F}(gA) = \mathcal{F}(A) \quad (5)$$

is valid with $g \in \mathcal{G}$, if gA is the set to be moved.

- Continuity: if for a sequence $K_n \rightarrow K$ is valid for $n \rightarrow \infty$, then

$$\mathcal{F}(K_n) \rightarrow \mathcal{F}(K) \quad (6)$$

converges as well. So, an approximation of the convex set K by the sequence K_n is reflected in an approximation in the functional equation. This continuity is (amongst others) an important property for the description of shape if real structures are imaged by digital techniques.

Even though Hadwiger's theorem is valid for an arbitrary dimension d of space, we are mainly interested in the two- and three-dimensional cases where the Minkowski functionals can be expressed by well-known geometrical quantities. In three dimensions, one obtains four Minkowski functionals M_0, \dots, M_3 , which are connected to geometric quantities such as volume, surface area and curvature integrals by the relations given in table 1. In two dimensions, the Minkowski functionals are the covered area, the boundary length between the homogeneous domains and the Euler characteristic, i.e. the number difference of connected domains and holes.

2.2. Grey-scale images

The purpose of this paper is to present an algorithm that can determine the Minkowski functionals fast and reliably for grey-scale images. A convenient method to characterize quantitatively such images is the histogram $\#(\rho)$, i.e. the number of pixels with grey value ρ . For getting more detailed information about the morphology, the images can be analysed separately for every grey-scale value. Therefore, a threshold ρ is defined which can take values between the minimum, 0, and the maximum grey-scale, 255 in our case. After choosing a threshold value, all the pixels with smaller grey values are set to black, the others to white, cf figure 3. Hence, a grey-scale image $\hat{\rho}(\vec{x})$ with, for example, 256 grey shades (a 3D topography) is disassembled into 256 two-dimensional binary images \mathcal{D}_ρ (also

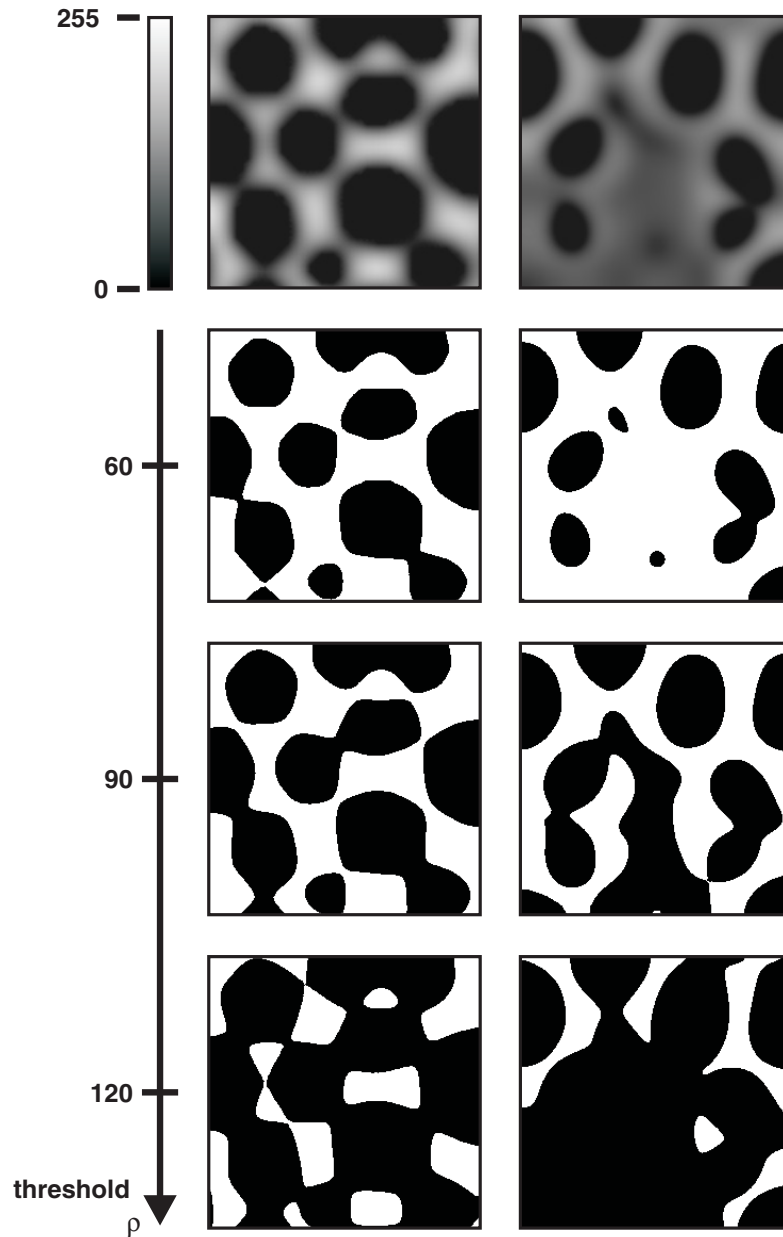


Figure 3. Dewetting pattern analysis. Top row: two grey-scale images of a later (left) and an earlier stage (right) of a dewetting film as obtained by finite element simulations (taken from [1]). Rows 2–4 show binary images created from the respective grey-scale images by setting a threshold value ρ to 60, 90 and 120 of 256 shade of grey.

denoted as isoheight planes). It is obvious that the Minkowski functionals $M_\nu(\mathcal{D}_\rho)$ of these excursion sets, i.e. the geometric quantities for a single isoheight plane drastically depend on the threshold ρ . For high values of ρ , the regions of maximum height can be studied, while for lower thresholds, one can analyse deep valleys of the structure. The covered area $M_0(\mathcal{D}_\rho)$ equals the cumulative histogram $\sum_{\rho'=\rho}^{255} \#(\rho')$ of the grey-scale image. The

Table 2. Impact of different square sizes (see figure 4) on the estimators of covered area, boundary length and Euler characteristic of a circle. The sector number i corresponds to the notation in figure 4(b). For comparison, the values for a circle are also given.

Sector i	Side length a_i/R	Covered area F	Boundary length U	Euler char. χ
1	4/7	$16a_1^2 \approx 5.2R^2$	$16a_1 \approx 9.1R$	1
2	2/7	$52a_2^2 \approx 4.2R^2$	$32a_2 \approx 9.1R$	1
3	1/7	$172a_3^2 \approx 3.5R^2$	$56a_3 = 8R$	1
4	1/14	$648a_4^2 \approx 3.3R^2$	$112a_4 = 8R$	1
Exact value		$\pi R^2 \approx 3.1R^2$	$2\pi R \approx 6.2R$	1

challenge is now to determine the other Minkowski functionals, dependent on the applied threshold ρ .

2.3. Discretized Minkowski functionals

The covered area $F = M_0$ of an image consisting of pixels is straightforward to compute. For a unit circle, the influence of different sizes of square pixels is shown in figure 4(a). It is evident that the computed value converges to the *true* continuous value as the size of the square gets smaller.

In the 2D space of the isoheight planes, the determination of the boundary length $U = 2\pi M_1$ is not as straightforward as for the covered area. In figure 4(b), we show how to estimate the boundary of a circle of radius R . If the squares have the size $a = 4/7 R$ as shown in sector 1 in the upper left corner, an upper estimator for the boundary length of the circle is $16a \approx 9.14 R$. When moving clockwise, the square width decreases in the next sectors, each by a factor of 2. Similarly, an upper estimator for the area is gained.

Table 2 gives the results for the upper estimators if the side length a of a grid cell is cut in half from one sector to the next. It is evident that this procedure is not capable of yielding an estimator for the boundary length, due to the lack of adjusting to the roundness of the object. Hence, the perimeter of a circle described by smaller and smaller squares approaches the value $8R$ but cannot converge to the true value $2\pi R \approx 6.28$ which involves the transcendental number π even if a is infinitely small. This problem is the well-known impossible task of how to find a *quadrature of a circle* [17].

A first attempt to improve the accuracy of determining the values for the metric quantities, area $F = M_0$ and boundary length $U = 2\pi M_1$ is to approximate the boundary by isosceles triangles as parts of the elementary squares. The 16 suitable pixel configurations of the so-called marching square algorithm that can occur are shown in figure 6 together with their representation by domains (black/white regions) in the Euclidean space. To illustrate the algorithm, let us apply this idea to sector 1 of the circle sketched in figure 4(b). Instead of the three pixels in sector 1, we now use squares #4, #6 and #12 to approximate the upper left part of the boundary. For two different side lengths of the squares, the result for approximating the circle is shown in figure 4(d). Applying this discretization scheme the estimator for the boundary of a circle is $U \approx 6.62R$ —a slightly improved value than for approximation only by squares as in figure 4(b) but not close to the continuous value. Yet this procedure based on the 16 different configurations

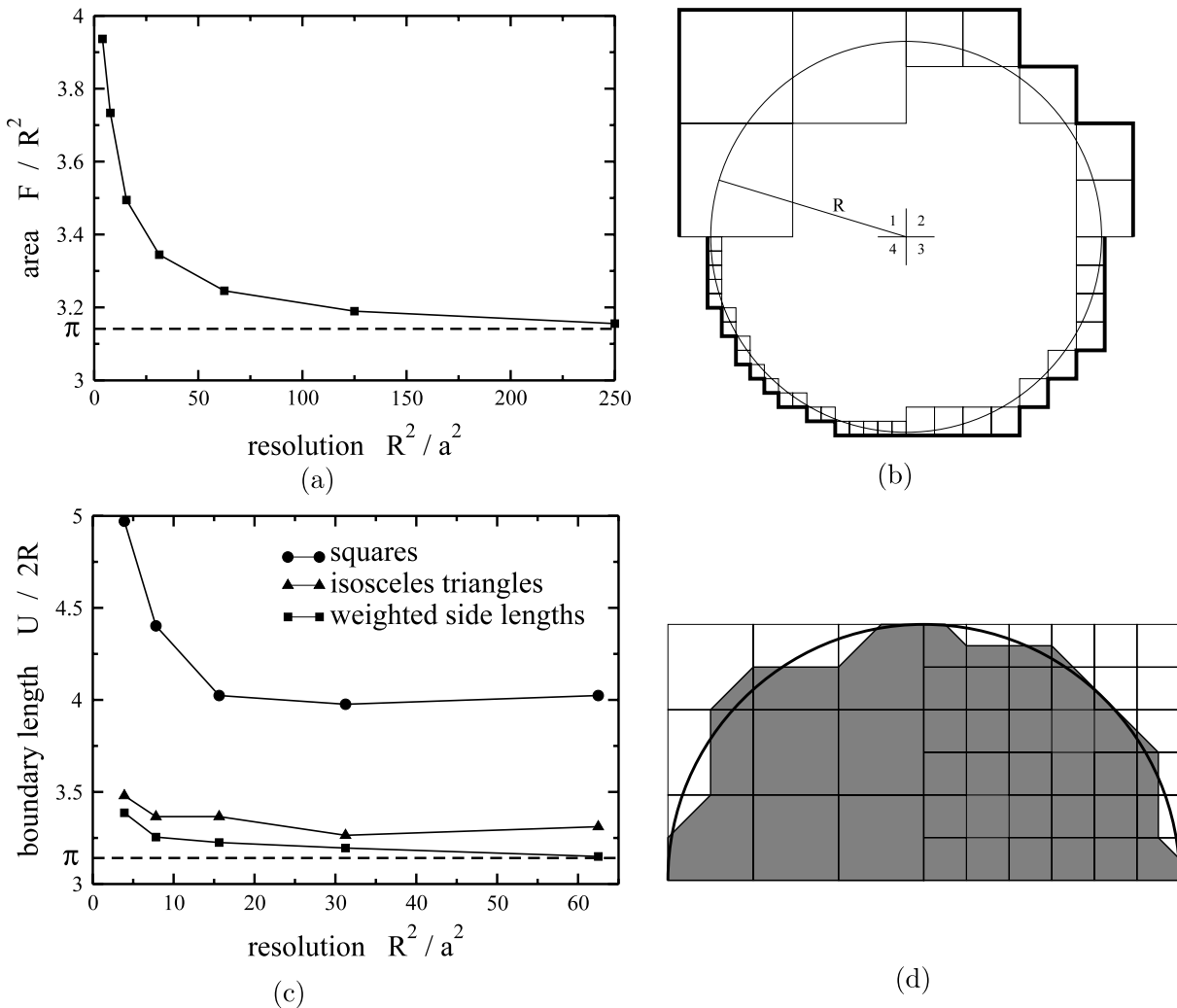


Figure 4. Discretized images require some care in determining continuous geometric quantities: (a) the covered area $F = M_0(A)$ is insensitive to the discretization method, so that the computed value always converges to the value πR^2 that is expected in the limit of small pixel size a . (b) The boundary length $U = 2\pi M_1(A)$ of a circle for different sizes of a square grid does not converge to its continuous value. From each sector $i = 1, \dots, 4$ to the next the grid distance a_i is decreased by a factor of 2. The thick solid lines in the respective sectors represent an upper estimator for the boundary length of the circle. The results are shown in table 2. (c) The boundary length $U = 2\pi M_1(A)$ of a circle depends strongly on the discretization technique: by squares as in (b) which does not converge to its continuous value for smaller grid sizes; by isosceles triangles as in (d) which improves the convergence for the boundary length but does not converge to the expected value; by weighted side length in a marching square algorithm as described in figure 7 which does converge. (d) Approximation of a circular arc by a discretization based on marching squares labelled in figure 6.

		- 1	0	0	0	- 1	
		+1				+1	
- 1			+1	0	+1		- 1
0			+1	- 1		0	
0			0			0	
0			+1	0	0	+1	
0						+1	- 1
	- 1	0	0	0	0	- 1	

Figure 5. The calculation of the Euler characteristic $\chi = \pi M_2$ requires only the number of signed corners, i.e. the sum of discretized curvature values -1 , 0 or 1 . The Euler characteristic χ does not depend on the details of the discretization as long as the topology of the pattern, i.e. the connectivity, is not changed due to a finite resolution of the structure.

in figure 6 also does not provide a satisfying result for the boundary length, even if the square size approaches zero. To obtain an even more precise value, which in principle can converge to the true continuous value, one may approximate the circle by a polygon which interpolates the structure between four pixels. This can be done by introducing weighted side lengths, where the position of the edge is linearly interpolated between two pixels. This procedure will be discussed in the following section 3 (see also figures 4 and 7).

In contrast to the area and the boundary length, the Euler characteristic $\chi = \pi M_2$ describes purely topological features of the structure without using a metric. It is a measure for the connectivity of the black and white components in a binary image. A white (black) component is a connected area of white (black) pixels. If N^w is the number of white components and N^b the number of black ones, the Euler characteristic is given by

$$\chi = N^w - N^b \quad (7)$$

is positive (negative), if there are many separate white (black) areas that are not connected to each other.

For the calculation of the Euler characteristic χ distances along the boundary are not important and the following procedure can be used [10]: the discretized curvature values -1 , 0 or 1 are assigned to every corner of a black pixel that is connected to at least one white pixel as can be seen in figure 5. A corner that is next to three white pixels is weighted by -1 and one that is next to one white square by 1 , other corners have no impact. The sum of these values divided by $4N$ (N is the number of pixels) equals the exact value of the Euler characteristic which is a topological measure for the connectivity

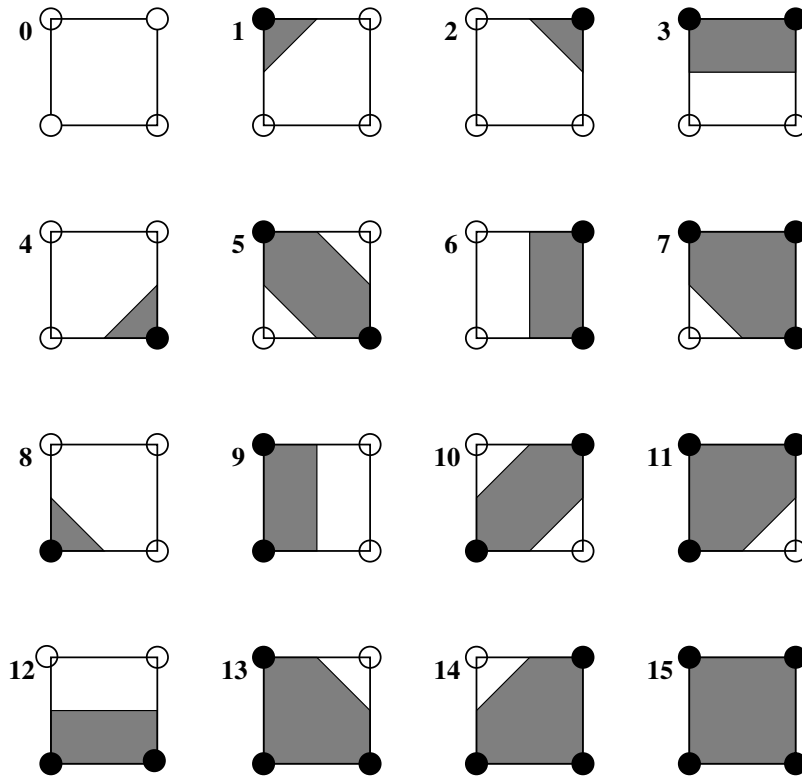


Figure 6. The 16 configurations of squares in the marching square algorithm. Filled circles denote that the grey-scale value of the pixel is larger than the threshold ρ , so that this point is inside the boundary of the structure.

of the structure. In two dimensions, χ is simply the difference between the connected components and the number of connected holes in the components.

Our approach to a more precise analysis method for the boundary length is to estimate the structure between two pixels by interpolating a value between them. We therefore refine the so-called marching square algorithm and move the boundary intersection along the edge to the angle whose grey value is closer to the threshold by using a linear interpolation. This idea is described in greater detail in the following section 3.

3. Marching cube/marching square algorithm for grey-scale images

As mentioned in the previous section 2, the Minkowski functionals are additive, so they can be calculated using a *divide-and-conquer* strategy: a complex situation is reduced to a few cases that can be treated separately and added afterwards.

We chose a modification of the *marching cube* algorithm that is normally used for displaying triangulated surface models from 3D medical data [18]. It approximates the real structure by creating volume elements called voxels. At first, a grid formed by cubes is created over the structure to be analysed. Any point of intersection of the straight lines with each other represents the structure at this spot. So one can decide if a point belongs to the structure or not. If this is done for all the points in the structure, one gets a simple surface representation of a complex structure by creating isosurfaces.

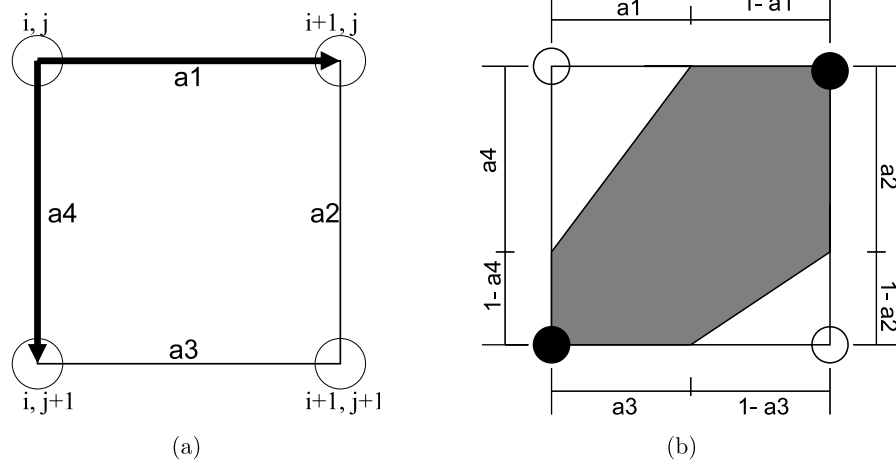


Figure 7. Weighted side lengths allow a more accurate measurement of threshold dependence than with the standard configurations of a marching square algorithm shown in figure 6: (a) describes the notations of the axis used in table 3; (b) configuration #10 of figure 6 is shown to illustrate the expression in table 3.

In our study, we use the two-dimensional version of a marching cube, the *marching square* algorithm. Here, instead of a cube a square *marches* on a 2D structure, forming a boundary. Thus again, for any point of the image one can decide if it belongs to the structure or not. A square can be located within the boundary of the object or outside, or it can be intersected by the boundary. This approach gives a good, or at least sufficient, representation for the whole structure. So, the contributions of each pixel (including its surrounding) to the Minkowski functionals can be added up to get one value for the whole image.

3.1. Marching square algorithm for Minkowski functionals

For the calculation of the covered area F and the boundary length U , the marching square algorithm can now be combined with an approach of weighted side lengths. As a first step, for each pixel of the image the suitable type of marching square shown in figure 6 has to be determined. This is done by deciding if the four pixels in figure 7(a) belong to the thresholded structure, i.e. if the grey-scale value is larger than the threshold ρ or not. As a second step, the weighted side lengths are calculated. If two neighbouring pixels (with distance 1) have the grey value c_i and c_j and only one of these pixels is within the structure, the intersection of the contour between the two pixels can be set by

$$a = \frac{c_i - \rho}{c_i - c_j}. \quad (8)$$

As an example, type #10 shown in figure 6 is redrawn in figure 7(b) with weighted side lengths. The other configurations of figure 6 can be treated accordingly. The threshold ρ decides up to which grey value a pixel is counted as belonging to the structure. This definition is useful because the intersection is then moved to the pixel, the grey value of which is closer to the threshold. Also, if the threshold is set right in the middle of the two grey values ($\rho = (c_i + c_j)/2$), one obtains $a = 1/2$. So, the separation scheme using

Table 3. Contribution of each of the 16 types of marching squares sketched in figure 6 by using weighted side lengths. The intersections a_1, \dots, a_4 are explained in figure 7.

Type c	F_c	U_c	χ_c
0	0	0	0
1	$\frac{1}{2}a_1a_4$	$\sqrt{a_1^2 + a_4^2}$	$\frac{1}{4}$
2	$\frac{1}{2}(1 - a_1)a_2$	$\sqrt{(1 - a_1)^2 + a_2^2}$	$\frac{1}{4}$
3	$a_2 + \frac{1}{2}(a_4 - a_2)$	$\sqrt{1 + (a_4 - a_2)^2}$	0
4	$\frac{1}{2}(1 - a_2)(1 - a_3)$	$\sqrt{(1 - a_2)^2 + (1 - a_3)^2}$	$\frac{1}{4}$
5	$1 - \frac{1}{2}(1 - a_1)a_2 - \frac{1}{2}a_3(1 - a_4)$	$\sqrt{(1 - a_1)^2 + a_2^2} + \sqrt{a_3^2 + (1 - a_4)^2}$	$\frac{1}{2}$
6	$(1 - a_3) + \frac{1}{2}((1 - a_1) - (1 - a_3))$	$\sqrt{1 + (a_3 - a_1)^2}$	0
7	$1 - \frac{1}{2}a_3(1 - a_4)$	$\sqrt{a_3^2 + (1 - a_4)^2}$	$-\frac{1}{4}$
8	$\frac{1}{2}a_3(1 - a_4)$	$\sqrt{a_3^2 + (1 - a_4)^2}$	$\frac{1}{4}$
9	$a_1 + \frac{1}{2}(a_3 - a_1)$	$\sqrt{1 + (a_3 - a_1)^2}$	0
10	$1 - \frac{1}{2}a_1a_4 - \frac{1}{2}(1 - a_2)(1 - a_3)$	$\sqrt{a_1^2 + a_4^2} + \sqrt{(1 - a_2)^2 + (1 - a_3)^2}$	$\frac{1}{2}$
11	$1 - \frac{1}{2}(1 - a_2)(1 - a_3)$	$\sqrt{(1 - a_2)^2 + (1 - a_3)^2}$	$-\frac{1}{4}$
12	$(1 - a_2) + \frac{1}{2}((1 - a_4) - (1 - a_2))$	$\sqrt{1 + (a_2 - a_4)^2}$	0
13	$1 - \frac{1}{2}(1 - a_1)a_2$	$\sqrt{(1 - a_1)^2 + a_2^2}$	$-\frac{1}{4}$
14	$1 - \frac{1}{2}a_1a_4$	$\sqrt{a_1^2 + a_4^2}$	$-\frac{1}{4}$
15	1	0	0

isosceles triangles as parts of the squares (figure 6) is just a special case of this more general approach.

To test the algorithm, results of three different discretization schemes have been computed for a model image: a black circle on a white background where the two-colour image has been modified such that the boundary was smoothed by standard image processing algorithms. The smoothing width is much less than any grid size of the discretization scheme, so that the smoothing has no visible effect on the measured area F . The results are shown in figure 4(c). It can be clearly seen that the computed value converges to the expected value π only when using weighted side lengths in a marching square algorithm. Without smoothing the weighted side lengths are irrelevant and the algorithm converges for a circle to a slightly larger value ≈ 3.3 compared to $\pi \approx 3.14$.

The algorithm does the calculation in two steps per square: first, for each corner of the square, it is decided if it belongs to the structure or not. That way, a binary image is produced. So, one of the types displayed in figure 6 can be assigned to all the squares that make up an image. Second, the areas and lengths are computed for each square individually by using the weighted side lengths. In this step, the grey-scales are used again. In table 3 the contribution of the 16 configurations to the area F , the boundary length U and the Euler characteristic χ are shown by using the weighted side lengths in figure 6. Finally, using the additivity of the Minkowski functionals, the overall value of the three measures is the sum of all the contributions of the squares. The algorithm uses only information inside a square with four pixels at its corners. Therefore

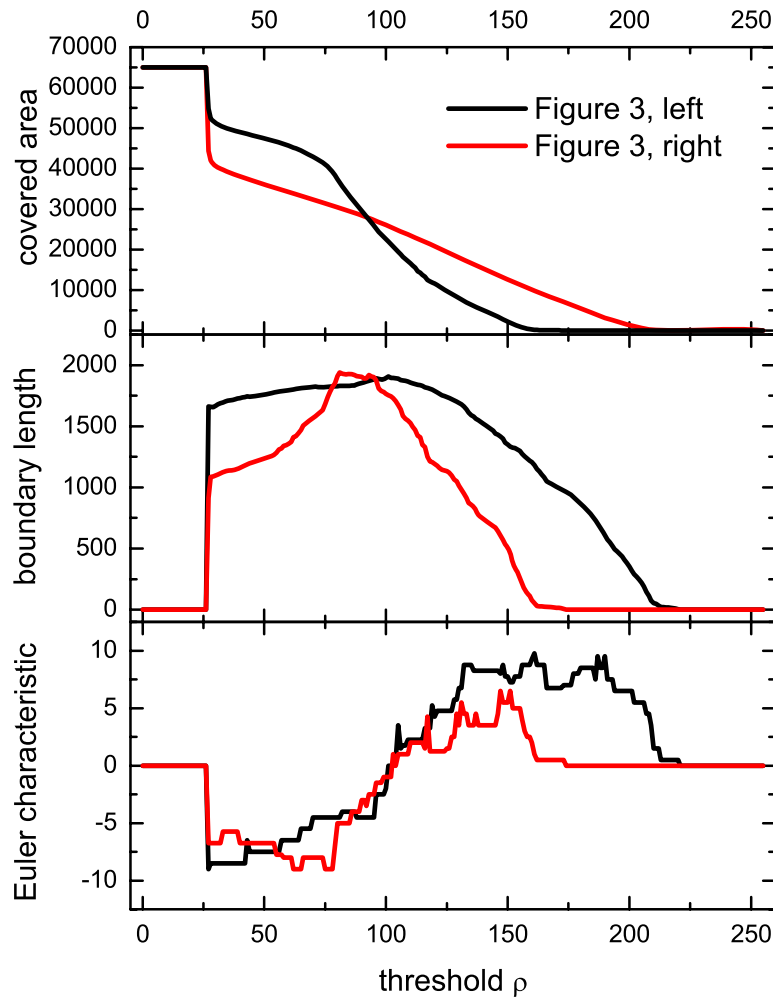


Figure 8. Minkowski functions $M_\nu(\mathcal{D}_\rho)$, i.e. covered area M_0 , boundary length M_1 and Euler characteristic M_2 as obtained by the marching square algorithm. The graphs are the results of the images shown in figure 3.

no boundary corrections are needed since the algorithm uses only data within the image and not interfaces generated at the edges of squares, for instance.

Doing this procedure for all thresholds, the Minkowski functionals $M_\nu(\mathcal{D}_\rho)$ of the thresholded images are functions $M_\nu(\rho)$ of the threshold ρ . In figure 8 these Minkowski functions are presented for the two examples shown in figure 3. They characterize the shape and connectivity of the grey-scale images and serve as a *fingerprint* of the structure. Details about how these measures can be used in practise to characterize grey-scale images are given in section 5. It is straightforward to relate them to more familiar quantities in image analysis, for example to the grey-scale histogram

$$\#(\rho) = -\frac{\partial M_0(\rho)}{\partial \rho}, \quad (9)$$

to the mean value of the grey-scale images

$$\rho_0 = \frac{\int d\rho \rho M_1(\rho)}{\int d\rho M_1(\rho)} \quad (10)$$

and to the standard deviation, i.e. the mean squared roughness

$$\sigma = \frac{\int d\rho (\rho - \rho_0) M_1(\rho)}{\int d\rho M_1(\rho)}. \quad (11)$$

However, the strength of $M_\nu(\rho)$ is the interpretation as geometric and topological measures of iso-grey-scale contours which will be discussed below in section 4.

3.2. Implementation

The first implementation of the algorithm was done in Java, which was chosen for its excellent portability of the source code and for its ease of extension. We also developed a platform-independent GUI (graphical user interface) that may facilitate the analysis described above. In the meantime, a command-line version written in C has been added. All source codes including explanations for their usage are provided for download on the [webpage](#).

Listing 1. Principle of the algorithm

```

for i := 0 to Width(ImageData) do begin
  for j := 0 to Height(ImageData) do begin
    // determine the case for each square
    if (Data[i][j] > rho) then case := case + 1;
    if (Data[i+1][j] > rho) then case := case + 2;
    if (Data[i+1][j+1] > rho) then case := case + 4;
    if (Data[i][j+1] > rho) then case := case + 8;

    // add Minkowski measures to sum, depending on selected case.
    if (case = 0) then ...

    ...

    if (case = 10) then
      begin
        // compute weighted side lengths
        a1 := (Data[i][j] - rho) / (Data[i][j] - Data[i+1][j]);
        a2 := (Data[i+1][j] - rho) / (Data[i+1][j] - Data[i+1][j+1]);
        a3 := (Data[i][j+1] - rho) / (Data[i][j+1] - Data[i+1][j+1]);
        a4 := (Data[i][j] - rho) / (Data[i][j] - Data[i][j+1]);

        // add contribution of this square to Minkowski measures
        f := f + 1 - 0.5 * a1 * a4 + 0.5 * (1 - a2) * (1 - a3);
        u := u + sqrt(a1 * a1 + a4 * a4) + sqrt((1 - a2) * (1 - a2) + (1 - a3) * (1 - a3));
        chi := chi + 0.5;
      end;

    if (case = 11) then ...

  end; // j - loop
end; // i - loop

```

To explain the principle, the algorithm is sketched in pseudocode in listing 1. In $\text{Data}[i][j]$, the grey code (ranging from 0 to 255 or from black to white in our examples) of the image in column i and row j is stored; ρ denotes the threshold ρ . At first, the software decides which of the 16 types shown in figure 6 is present at the position $[i][j]$ and the neighbours in the positive direction (see figure 7(a)).

Using the Heaviside function $\Theta(x)$, the type c (from $0 \dots 16$) can be computed by

$$c = \Theta(\text{Data}[i][j+1] - \rho)2^3 + \Theta(\text{Data}[i+1][j+1] - \rho)2^2 + \Theta(\text{Data}[i+1][j] - \rho)2^1 + \Theta(\text{Data}[i][j] - \rho)2^0. \quad (12)$$

This corresponds to a four-bit code. In the source code, this is done in lines 4–7. Having this information, the calculation has to be done separately using the formula listed in table 3. As an example, type #10 (that is also sketched in figure 7) is shown here in more detail. All the other configurations are treated accordingly and can be found in the source code provided on the [webpage](#). In lines 17–20, the weighted side lengths are computed using equation (8). Using these values, the software adds the contribution of—in our example—type #10 square to the Minkowski functionals covered area F , boundary length U and Euler characteristic χ . As mentioned in section 2.1, the Minkowski functionals are additive, so that a loop over all pixels (counted by the variables i and j) results in the overall value of F , U and χ .

To evaluate the accuracy of the algorithm, one may compare numerical results obtained by this code with analytically known results for stochastic models of grey-scale images. In section 4, we discuss typical grey-scale images obtained by realizations of standard stochastic models where mean values of Minkowski functionals can be computed explicitly.

4. Stochastic geometry: models for random spatial structures

Although the functional dependence of the Minkowski functionals on the threshold ρ can be quite complex (notice the shape differences visible in the images shown in figures 3, 12), one can find explicit expressions for standard models of stochastic geometries, which depend only on a finite number of model parameters (for a review on integral geometry see [5, 15]). Comparing analytic results with experimental data one may numerically determine these parameters which finally can be used for statistical tests. The simplest model is a lattice of pixels with random grey-scale values, i.e. identically and independently distributed values. At the other extreme one can study Gaussian random fields on the two-dimensional continuous Euclidean space \mathbb{R}^2 . In general one can combine both approaches to a Gaussian lattice model which takes into account the pixel structure of datasets and intrinsic correlations of the pattern's grey-scale.

The grey-scale image may be parametrized by a single-valued *density field* $\hat{\rho}(\vec{x})$ of the spatial coordinates $\vec{x} \in \Omega \subset \mathbb{R}^2$ inside a domain (observation window) Ω of area $|\Omega|$. The excursion set \mathcal{D}_ρ over a given threshold ρ is defined as the binary image $\mathcal{D}_\rho = \Theta(\hat{\rho}(\vec{x}) - \rho)$ with the Heaviside step function $\Theta(x)$. We define the averaged Minkowski functions by

$$m_\nu(\rho) = \frac{1}{|\Omega|} M_\nu(\mathcal{D}_\rho) \quad (13)$$

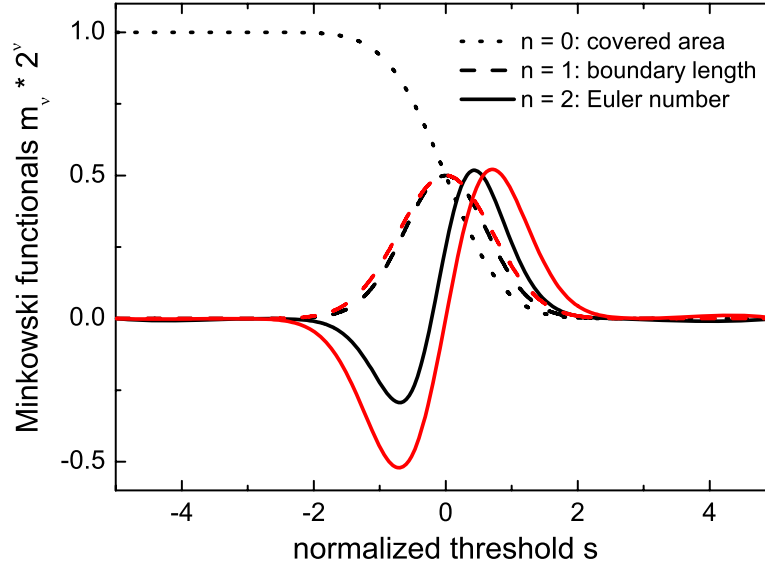


Figure 9. Minkowski functionals $m_\nu(\rho)$ as a function of the normalized threshold $s = \rho/\sqrt{2\sigma^2}$ for the random lattice model (black; see equation (15)) and the Gaussian random field model (red; see equation (25)). Although the area $m_0(\rho)$ is equal for different models, one may use the boundary length $m_1(\rho)$ and the Euler characteristic $m_2(\rho)$ to distinguish the models.

which depend on the threshold ρ . In the following, we calculate these function for three different models, so that we can compare them in section 5 with measured values for reaction–diffusion systems (see section 5.2 and figure 2(b)) and for dewetting processes (see section 5.3 and figure 1).

4.1. Random lattice model

If the grey-scale ρ of each pixel is identically and independently distributed (i.i.d.) with the probability density

$$p(\rho) = \frac{1}{\sqrt{2\pi}\sigma} \exp\left\{-\frac{1}{2}\frac{\rho^2}{\sigma^2}\right\} \quad (14)$$

and variance σ^2 , one finds immediately

$$\begin{aligned} m_0^{(L)}(\rho) &= \frac{1}{2} \left(1 - \operatorname{erf}\left(\frac{\rho}{\sqrt{2}\sigma}\right)\right) \\ m_1^{(L)}(\rho) &= m_0(\rho)(1 - m_0(\rho)) \\ m_2^{(L)}(\rho) &= m_0(\rho)(1 - m_0(\rho))(1 - m_0(\rho) - m_0^2(\rho)) \end{aligned} \quad (15)$$

with the error function $\operatorname{erf}(x) = 2/\sqrt{\pi} \int_0^x dt e^{-t^2}$. These Minkowski functions are shown in figure 9 with the normalized threshold $s = \rho/\sqrt{2\sigma^2}$.

4.2. Gaussian random field model

A Gaussian random field is an excellent stochastic model for many geometrical features observed in physical data, for the cosmic background radiation field [5], for capillary waves or for spinodal dewetting in the linear dynamic regime [1]. For convenience, one may study Gaussian random fields in Fourier space in which the modes for different wavevectors decouple. To this end we introduce the Fourier-transformed functions:

$$\tilde{\rho}(\vec{q}) = \int_{\mathbb{R}^2} d^2\vec{x} e^{-i\vec{q}\cdot\vec{x}} \hat{\rho}(\vec{x}) \quad \text{and} \quad \hat{\rho}(\vec{x}) = \int_{\mathbb{R}^2} \frac{d^2\vec{q}}{(2\pi)^2} e^{i\vec{q}\cdot\vec{x}} \tilde{\rho}(\vec{q}). \quad (16)$$

One may assume that the modes $\tilde{\rho}(\vec{q})$ are identically and independently distributed, and that the probability $P[\tilde{\rho}] \sim \exp(-|\tilde{\rho}|^2/\tilde{\sigma}^2)$ of the amplitudes $\tilde{\rho}(q)$ is Gaussian for a *grey-value wave* of wavevector q . Then, the Gaussian random field model can be defined by the explicit expression

$$P[\tilde{\rho}(q)] = \frac{1}{\pi\tilde{\sigma}^2(\vec{q})} e^{-(|\tilde{\rho}(q)|^2)/(\tilde{\sigma}^2(\vec{q}))} \quad (17)$$

with the wavevector-dependent variance $\tilde{\sigma}^2(\vec{q})$. Mean values $\langle A \rangle$ for functionals $A[\hat{\rho}(\vec{x})]$ of the random field can straightforwardly be calculated by

$$\langle A \rangle_{\tilde{\sigma}(\vec{q})} = \int \mathcal{D}\hat{\rho} A[\hat{\rho}(\vec{x})] \quad (18)$$

where the abbreviation

$$\int \mathcal{D}\hat{\rho} = \prod_{\vec{q} \in \mathbb{R}^2/2} \int_{-\infty}^{\infty} d(\text{Re } \tilde{\rho}(\vec{q})) \int_{-\infty}^{\infty} d(\text{Im } \tilde{\rho}(\vec{q})) \frac{1}{\pi\tilde{\sigma}^2(\vec{q})} e^{-((\text{Re } \tilde{\rho}(\vec{q}))^2 + (\text{Im } \tilde{\rho}(\vec{q}))^2)/(\tilde{\sigma}^2(\vec{q}))} \quad (19)$$

denotes the integration measure for the field degrees of freedom which solely depends on $\tilde{\sigma}(\vec{q})$. Because of the relation $\tilde{\rho}(-\vec{q}) = \tilde{\rho}^*(\vec{q})$, the product in equation (19) runs only over suitably discretized vectors \vec{q} in the half-space $\mathbb{R}^2/2$. One finds the spectrum $\langle \tilde{\rho}(\vec{q}) \tilde{\rho}(\vec{q}') \rangle = (2\pi)^2 \delta(\vec{q} + \vec{q}') \tilde{\sigma}^2(\vec{q})$ which is usually used to characterize a grey-scale image. Therefore, the Fourier transformation $\tilde{g}(\vec{q})$ of the correlation function $g(\vec{r}) = \langle (\hat{\rho}(\vec{x}) - \bar{\rho})(\hat{\rho}(\vec{x} + \vec{r}) - \bar{\rho}) \rangle$ is

$$\tilde{g}(\vec{q}) = \int_{\mathbb{R}^2} d\vec{r} g(\vec{r}) e^{-i\vec{q}\cdot\vec{r}} = \int \frac{d\vec{q}'}{(2\pi)^2} e^{i(\vec{q} + \vec{q}')\cdot\vec{r}} \langle \tilde{\rho}(\vec{q}) \tilde{\rho}(\vec{q}') \rangle = \tilde{\sigma}^2(\vec{q}) \quad (20)$$

and thus equals the spectrum $\tilde{\sigma}(\vec{q})$ of a Gaussian random field. The inverse is

$$g(\vec{r}) = \int_{\mathbb{R}^2} \frac{d\vec{q}}{(2\pi)^2} \tilde{\sigma}^2(\vec{q}) e^{i\vec{q}\cdot\vec{r}} = \int \frac{dq}{2\pi} q \tilde{\sigma}^2(q) J_0(q|\vec{r}|) \quad (21)$$

where the last equation is only valid for an isotropic spectrum $\tilde{\sigma}^2(\vec{q}) = \tilde{\sigma}^2(|\vec{q}|)$. In particular, one obtains the integrals of the spectrum, i.e. the variance of the grey values and of their derivatives:

$$\begin{aligned} \sigma^2 &= g(\vec{r}=0) = \int_{\mathbb{R}^2} \frac{d\vec{q}}{(2\pi)^2} \tilde{\sigma}^2(\vec{q}) \\ k^2 &= -\frac{g''(\vec{r}=0)}{2\pi\sigma^2} = \frac{1}{2\pi} \int_{\mathbb{R}^2} \frac{d\vec{q}}{(2\pi)^2} \vec{q}^2 \tilde{\sigma}^2(\vec{q}) \bigg/ \int_{\mathbb{R}^2} \frac{d\vec{q}}{(2\pi)^2} \tilde{\sigma}^2(\vec{q}) \end{aligned} \quad (22)$$

which are the most convenient and prominent measures to characterize the distribution of the grey-scales $\hat{\rho}(\vec{r})$ in an image. A main problem in using the spectrum $\tilde{\sigma}^2(\vec{q})$ to characterize a grey-scale image is its strong dependence on boundaries and stochastic noise which can be dominant in small images usually measured by AFM or optical microscopy.

The mean Minkowski functionals of the exclusion set is given by

$$m_\nu^{(GF)}(\rho) = k^\nu \frac{\omega_d}{\omega_{d-\nu}\omega_\nu} H_{\nu-1} \left(\frac{\rho - \rho_0}{\sigma} \right) \quad (23)$$

(see [19]) with the Hermite functions

$$H_\nu(x) = \frac{1}{\sqrt{2\pi}} \left(-\frac{\partial}{\partial x} \right)^\nu e^{-(1/2)x^2} \quad (24)$$

and the volume ω_d of a d -dimensional unit ball (see equation (1)). Thus, no matter what the correlation function $g(\vec{r})$ looks like, the mean values of the Minkowski functionals are given by only three parameters ρ_0 , σ and k :

$$\begin{aligned} m_0^{(GF)}(\rho) &= \frac{1}{2} - \frac{1}{\sqrt{2\pi}\sigma} \int_0^{\rho-\rho_0} dt e^{-(1/2)(t^2/\sigma^2)} = \frac{1}{2} \left(1 - \operatorname{erf} \left(\frac{\rho - \rho_0}{\sqrt{2}\sigma} \right) \right) \\ m_1^{(GF)}(\rho) &= \frac{k}{\sqrt{8\pi}} e^{-(1/2)((\rho-\rho_0)^2)/\sigma^2} \\ m_2^{(GF)}(\rho) &= \frac{k^2}{\sqrt{2\pi^3}\sigma^2} (\rho - \rho_0) e^{-(1/2)((\rho-\rho_0)^2)/\sigma^2}. \end{aligned} \quad (25)$$

In some cases it may be more convenient to define *effective* measures by an alternative normalization of the Minkowski functionals, namely

$$\begin{aligned} s(\rho) &= -\frac{\partial m_0(\rho)}{\partial \rho} \frac{1}{2\pi m_1(\rho)} \\ u(\rho) &= -\log(2\pi m_1(\rho)) \\ \kappa(\rho) &= \frac{m_2(\rho)}{2m_1(\rho)}. \end{aligned} \quad (26)$$

The advantage of these effective measures for spatial patterns compared to the original ones defined in equation (13) are the simplicity of the expression for a Gaussian random field model, where the effective measures are

$$\begin{aligned} s^{(GF)}(\rho) &= s_0 \\ u^{(GF)}(\rho) &= u_0 + u_2(\rho - \rho_0)^2 \\ \kappa^{(GF)}(\rho) &= \kappa_1(\rho - \rho_0) \end{aligned} \quad (27)$$

with $s_0 = 1/(\pi\sigma k)$, $u_0 = -\log k\sqrt{\pi/2}$, $u_2 = 1/(2\sigma^2)$ and $\kappa_1 = k/(\pi\sigma)$. Thus, one finds polynomials up to second order, i.e. a constant $s(\rho)$, a linear $\kappa(\rho)$ and a quadratic $u(\rho)$, with only five scalar and positive coefficients.

For Gaussian grey-scale images, one can measure the roughness σ^2 (according to equation (11)) simply by determining the coefficients for the effective Minkowski functionals, which should consistently give the same value. This can be used to test if the grey-scale image is indeed Gaussian.

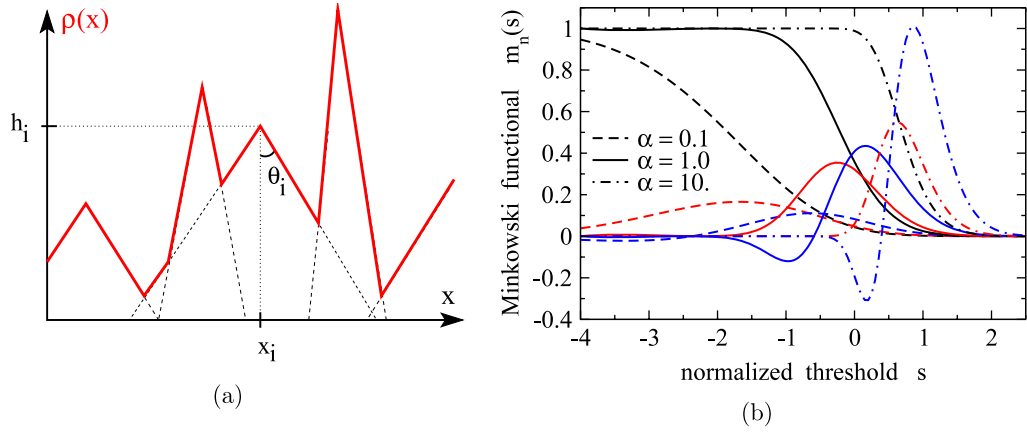


Figure 10. Maximum cone field model: a grey-scale pattern can be generated by taking the maximum value of randomly distributed cones of height h_i , opening angle θ_i and position \vec{x}_i . (b) For $\theta(h) = \theta_0$ and $P(h) = \exp\{-h^2/2\sigma^2\}/\sqrt{2\pi\sigma^2}$ the Minkowski functions $m_\nu^{(MC)}(\rho)$ (see equation (32), area (black), boundary length (red), Euler characteristic (blue)) depend strongly on the dimensionless parameter $\alpha = (2/\sqrt{\pi})(n\sigma^2/(\tan\theta_0))$. Here, the normalized threshold $s = \rho/\sqrt{2\sigma^2}$ and the normalized functions $m_\nu(s) = (\sqrt{2\sigma^2}/\tan\theta_0)^\nu m_\nu^{(MC)}(\rho/\sqrt{2\sigma^2})$ are used.

In order to test a grey-scale image for features of a Gaussian random field model one may measure the quantities

$$X := \frac{e^{-2u_0}s_0}{\kappa_1} = \frac{\pi}{2} \quad \text{and} \quad Y := \frac{\kappa_1 s_0}{u_2} = \frac{2}{\pi^2} \quad (28)$$

which are independent of the specific correlation function, i.e. do not depend on the details of a Gaussian random field, but are sensitive to non-Gaussian features. For instance, the effective Minkowski functionals are not polynomials for the random lattice model discussed above in equation (15). However, for the applications discussed in the following section (i.e. for the turbulent Turing pattern shown in figures 2(b) and 12, as well as for the dewetting process of thin films in the early regime (see figures 1 and 13), we find not only the polynomials, but also the Gaussian values for X and Y given by equation (28). Such a test on Gaussian behaviour may be important also in astroparticle physics and cosmology (see [20, 21]), where the search for non-Gaussianity in the cosmic background radiation field is one of the most important tasks. It can be illustrated that non-Gaussian features are very common in grey-scale images by calculating mean values of Minkowski functionals for another stochastic geometry model.

4.3. Maximum cone field model

Let us consider a Poisson distribution of points $\vec{x}_i \in \mathbb{R}^d$ with density n and a function $\phi_i(\vec{x})$ which is attached at each point \vec{x}_i . For instance, a cone i of height h_i and opening angle θ_i (see figure 10) is represented by

$$\phi_i(\vec{x} - \vec{x}_i) = h_i - |\vec{x} - \vec{x}_i| \tan \theta_i. \quad (29)$$

For convenience, one may assume that the values of h_i are independently and identically distributed with probability $P(h)$ and that there is a deterministic relation $\theta(h)$ between opening angle and height of the cone. A random field $\rho(\vec{x})$ can now be defined by taking at each point \vec{x} the maximum value

$$\rho(\vec{x}) := \max_i \{\phi_i(\vec{x} - \vec{x}_i)\} \quad (30)$$

of all these cones. Taking a threshold, one finds that for each threshold this cone model is equivalent to a Boolean grain model with Poisson distributed grains K_i (see [22]). For the cone function given by equation (29) these grains are discs of radius $r_i = (h_i - \rho)/\tan \theta_i$. The mean values of Minkowski functionals for the discs at a given threshold are

$$\begin{aligned} \bar{M}_0(\rho) &= \pi \int_{\rho}^{\infty} dh P(h) \frac{(h - \rho)^2}{\tan^2 \theta(h)} \\ \bar{M}_1(\rho) &= \int_{\rho}^{\infty} dh P(h) \frac{h - \rho}{\tan \theta(h)} \\ \bar{M}_2(\rho) &= \frac{1}{\pi} \int_{\rho}^{\infty} dh P(h). \end{aligned} \quad (31)$$

Therefore, one finds for the mean values of Minkowski functionals for the union of these discs (for details, see [23])

$$\begin{aligned} m_0^{(MC)}(\rho) &= 1 - e^{-\bar{M}_0(\rho)n} \\ m_1^{(MC)}(\rho) &= \bar{M}_1(\rho)n e^{-\bar{M}_0(\rho)n} \\ m_2^{(MC)}(\rho) &= (\bar{M}_2(\rho)n - (\bar{M}_1(\rho)n)^2) e^{-\bar{M}_0(\rho)n} \end{aligned} \quad (32)$$

and the effective measures

$$\begin{aligned} s^{(MC)}(\rho) &= \frac{1}{\bar{M}_1(\rho)} \int_{\rho}^{\infty} dh P(h) \frac{h - \rho}{\tan^2 \theta(h)} \\ u^{(MC)}(\rho) &= \bar{M}_0(\rho)n - \log(2\pi \bar{M}_1(\rho)n) \\ \kappa^{(MC)}(\rho) &= \frac{\bar{M}_2(\rho)}{\bar{M}_1(\rho)} - \bar{M}_1(\rho)n. \end{aligned} \quad (33)$$

Thus, for $\theta(h) = \theta_0 = \text{constant}$ one finds a constant slope $s^{(MC)}(\rho) = \tan^{-1} \theta_0$ as in the case of a Gaussian random field discussed above. However, $\kappa^{(MC)}(\rho)$ is, in general, not a linear function in the threshold ρ , not even for $\theta(h) = \theta_0$.

This example demonstrates that the functional dependence of the effective Minkowski functionals is a significant feature of random fields, which can be used to discriminate between different models and to test, for example, for Gaussian random field behaviour. Therefore, one needs a reliable algorithm to calculate these functionals numerically as introduced in section 3.

5. Applications: pattern analysis with Minkowski functionals

As examples to illustrate the technique we consider the surface topologies gained by simulations of thin film dewetting, cf figure 1 and concentration patterns during spinodal

decomposition, cf figure 2(a) and in chemical reaction–diffusion systems, cf figure 2(b). The grey-scale corresponds to the height of the film or to the concentration of chemicals, respectively.

5.1. Pattern analysis of spinodal decomposition structures

To illustrate the importance of Gaussian random field models for physical processes we calculate the Minkowski functionals for the thresholded images of a phase-separating colloid–polymer mixture (see figure 2(a)). Details of the experiments are described in [8, 9]. The results of a morphological analysis by Minkowski functionals are shown in figure 11 for three thresholded grey-scale images of the video microscopy series. During the demixing process the maximum of the boundary length $m_1(\rho)$ is shifted from low values of the area m_0 to larger, and the minimum of $m_2(\rho)$ becomes deeper in time. After an initial build-up of the spinodal structures and before a gravity-driven flow begins, the shape of the coarsening patterns can be described by an Gaussian model, i.e. by equations (25). The deviation from Gaussian behaviour has two reasons: (i) in the beginning, the images are dominated by random noise in the fluorescence which occurs already in the stable liquid phases and which is only gradually superimposed by the inhomogeneities due to spinodal decomposition; (ii) in the late stage, the deviation marks the set-in of nonlinear dynamics in the spinodal decomposition. Of course, image artefacts such as non-uniform illumination may lead to a broadening of the histogram of the grey values and could have effects on the functional form of the Minkowski functionals. To circumvent this problem—at least partially—we have not used the actual threshold value ρ for the abscissa but the geometric quantity m_0 . Thus, a rescaling of the grey value of the pixels due to illumination has no effect anymore on the functional form of $m_1(m_0)$ and $m_2(m_0)$. Still, an inhomogeneous illumination can modify the functionals. However, in the images shown in figure 11 the image recording technique is the same for all time frames and the quantitative agreement with a homogeneous Gaussian model for frame 79 indicates a homogeneous illumination. Therefore, the visible deviation from a Gaussian model has its origin in the dynamics of spinodal decomposition. The advantage of an image analysis by Minkowski functionals is the unambiguous identification of non-Gaussian features which is important when comparing linear dynamic models with the experimental data.

5.2. Pattern analysis of chemical reaction–diffusion images

As a second example, we apply the concept of Minkowski functionals as morphological measures for thresholded grey-scale images on the analysis of Turing-type chemical patterns in a two-dimensional open spatial reactor with a chlorite–iodide–malonic acid reaction [10]. Details of the experiments are described in [31]. The occurrence of stationary spatial patterns in chemical reaction–diffusion systems was already predicted by Turing in 1952 and was extensively investigated since then by theoretical and numerical studies. The first experimental observation of stationary patterns in a gel reactor was in 1990. The patterns form in a thin, quasi-two-dimensional disc filled with polyacrylamide gel which prevents convection but allows for the diffusion of chemicals. Depending on the concentration of iodide I_3^- the system changes in colour from yellow to blue which is measured in digitized grey-scale images. Above critical values of the control parameters,

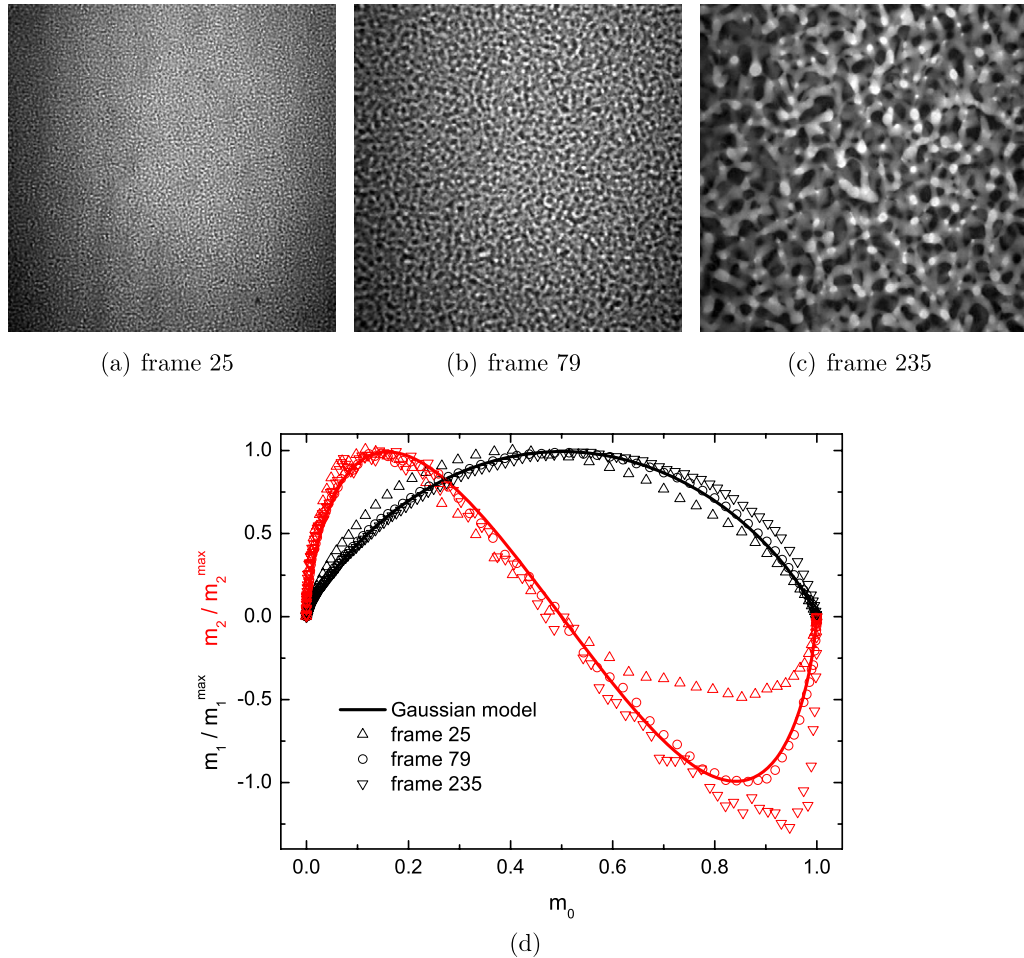


Figure 11. (a)–(c) Fluorescence microscopy images of spinodal fluid–fluid demixing (see [8, 9] and figure 2; courtesy Dirk Aarts and Henk Lekkerkerker). Random heterogeneous structures can be observed that are changing with time. (d) Analysis by Minkowski functionals: during an intermediate time window (e.g. frame 79) the structure can be well described by a Gaussian random field model. In the beginning (frame 25) as well as in the final coarsening before gravity sets in (frame 235) deviations from the Gaussian model are clearly visible. To compare the Gaussian model (solid lines) given by equation (25) the time dependence of prefactors in the data are removed by normalizing m_1 and m_2 to be their maximum values.

i.e. temperature and reagent concentrations, spatial patterns spontaneously emerge from a previously homogeneous system.

Three different types of patterns are reported in [31], a hexagonal structure of isolated dots, a lamellar stripe structure broken up into domains of different orientations and a structure of turbulent stripes, which change shape and orientation much faster than the usual moving of grain boundaries. Here, we focus solely on the image analysis of the latter structure. The Euler characteristic describes the topological structure of the pattern. It is negative (positive) if many disconnected black (white) components dominate the image. A

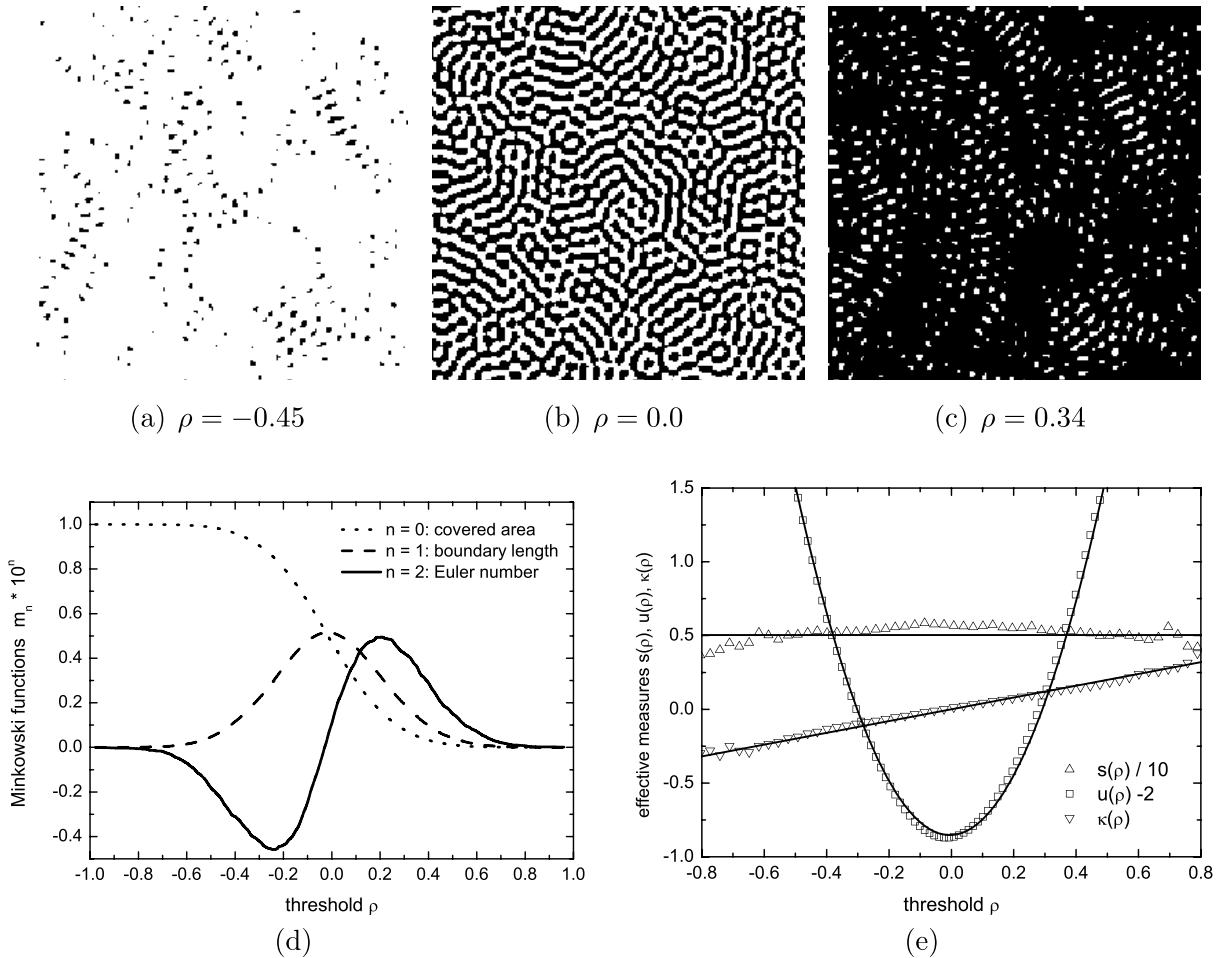


Figure 12. Chemical reaction–diffusion patterns: black and white images derived from the turbulent pattern shown in figure 2(b) at three different grey levels $\rho \in [-1, +1]$: (a) $\rho = -0.45$, (b) $\rho = 0.0$ and (c) $\rho = 0.34$. The image is white, where the grey level in figure 2(b) is larger than ρ . One can see clearly the different topologies of the images. At the threshold $\rho = 0.0$ the black and white components are highly connected, whereas at $\rho = -0.45$ ($\rho = 0.34$) many disconnected black (white) components occur. (d) The Minkowski functionals, i.e. the normalized area $m_0(\rho)$, the boundary length $m_1(\rho)$ and the Euler characteristic $m_2(\rho)$, as a function of the grey-scale threshold for the turbulent pattern shown in figure 2(b). (e) Effective measures according to equation (26) which are in good agreement with a Gaussian model (lines).

vanishing Euler characteristic indicates a highly connected structure with equal amounts of black and white components as for the pattern shown in figure 12(b), for instance.

In [10] the threshold dependence of the Minkowski functionals has been fitted, for example, by a hyperbolic tangent for the covered area $m_0(\rho)$. However, using the improved algorithm described above we obtain similar values, but a quantitative fit could be improved by using equations (25). Of course, the difference between an error function and a hyperbolic tangent cannot be seen in figure 12(d), but applying the

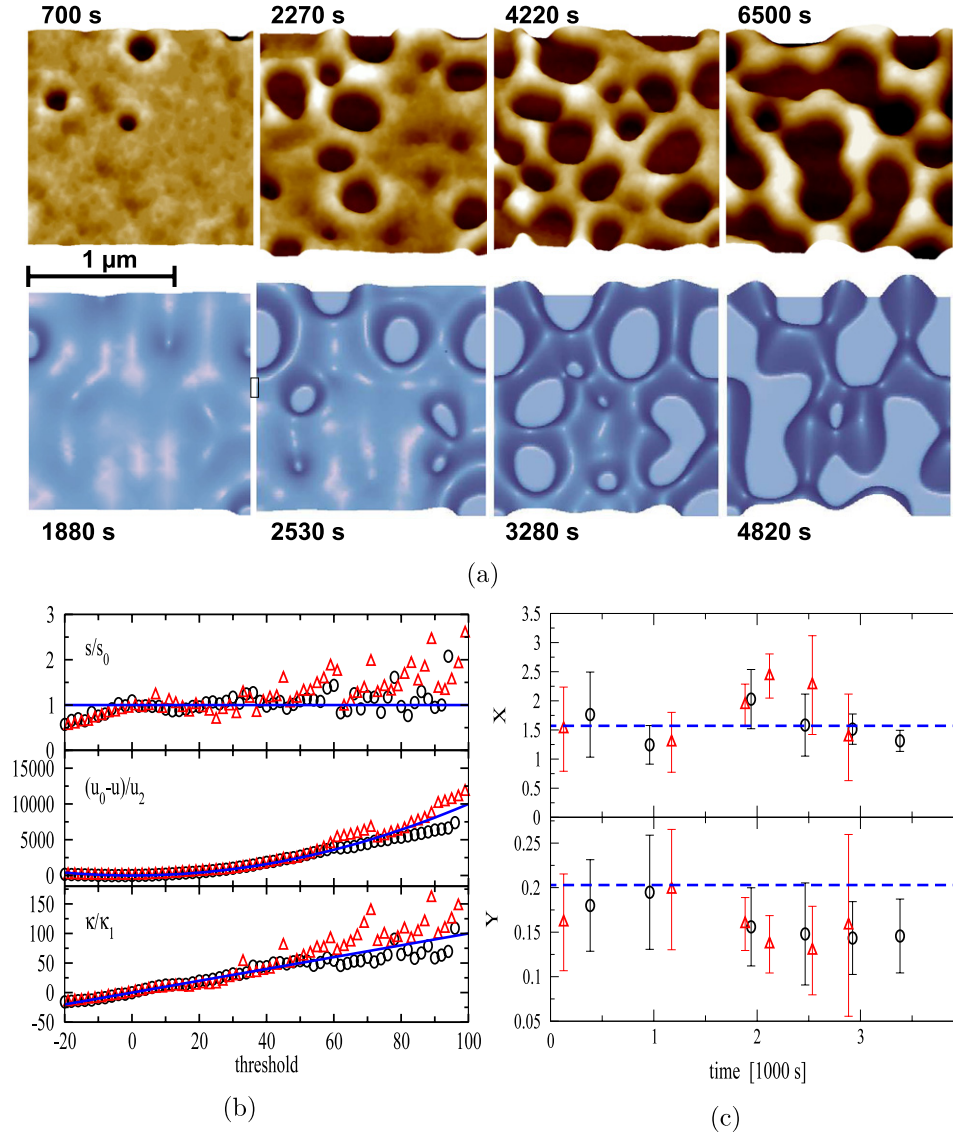


Figure 13. (a) Experimental (top) and simulated (bottom) dewetting morphology of a ultrathin film with identical system parameters: a 3.9 nm polystyrene film beads off an oxidized Si wafer (height range is 12 nm in both cases); experimental series were recorded by *in situ* AFM at $T = 53^\circ\text{C}$. It was shown in [1] that the complex spatial and temporal evolution of the rupture of films can be modelled in quantitative agreement with experiments. (b) The temporal evolution of the dewetting morphologies shown in (a) are analysed by Minkowski functionals $M_\nu(\rho)$ as a function of threshold ρ (experiments: black circles; simulations: red triangles; Gaussian model: blue lines). The effective measures $s(\rho)$, $u(\rho)$ and $\kappa(\rho)$ defined in equation (26) are fitted with a constant s_0 , a parabola $u_0 + u_2\rho^2$ and a linear function $\kappa\rho$, respectively. (c) The figure depicts for each time step the consistency check for X and Y as given by equation (28) for a Gaussian random field. For instance, from the fitted values $s_0 \approx 5.0$, $u_0 \approx 1.14$, $u_2 \approx 9.67$ and $\kappa_1 \approx 0.4$ one obtains the ratio $Y = (\kappa_1 s_0)/u_2 \approx 0.21$, which is in good agreement with the expected value $Y \approx 0.203$.

transformation to effective measures (26) one finds a good agreement with a Gaussian model (see figure 12(e)).

An excellent consistency check is provided by equation (28), i.e. by the ratios $X = e^{-2u_0} s_0 / \kappa_1 \approx 1.6$ and $Y = s_0 \kappa_1 / u_2 \approx 0.2$ which are close to the expected values $\pi/2$ and $2/\pi^2$, respectively. Thus, the morphological features of turbulent Turing patterns can be described by a Gaussian random field model introduced in section 4.2. This is not the case for the two other types of patterns, the lamellar stripes and hexagonal structures. The implication for modelling Turing patterns based on Gaussian random fields is not clear yet. However, the presented quantitative image analysis indicates a description by stochastic nonlinear equations and not by deterministic rate equations for reaction–diffusion systems.

5.3. Pattern analysis of dewetting morphologies in thin liquid films

The thickness $\rho(\vec{x})$ of, for example, insulating layers or photoresists for the fabrication of electronic chips now reaches the order of nanometres, resulting in new challenges to guarantee stability during production and use of the device. Given sufficient knowledge of system parameters such as dielectric constants ϵ and the Hamaker constants A of the participating media, the principal question of stability or instability of a given thin film can be answered by an effective interface potential $V(\rho) = \epsilon/\rho^8 - A/(12\pi\rho^2)$ which covers intermolecular forces beyond capillarity. Figure 13 displays atomic force microscopy (AFM) scans taken *in situ* of liquid polystyrene films beading off an oxidized Si wafer with $\epsilon = 6.3 \times 10^{-76} \text{ Jm}^6$ and $A = 2.2 \times 10^{-20} \text{ J}$, leading to an equilibrium thickness of $\rho = 1.3 \text{ nm}$ [32].

The knowledge of $V(\rho)$, however, is not sufficient to understand the evolution of a thin film instability in time. Since simulations based on molecular dynamics are numerically still too expensive, the theoretical framework for the description of fluid flow is based on a lubrication approximation of the Navier–Stokes equation:

$$\eta \partial_t \rho = \nabla \cdot (m(\rho) \nabla p) \quad (34)$$

for the film height $\rho(\vec{x}, t)$. Here, $\eta \approx 12\,000 \text{ Pas}$ is the viscosity, the augmented Laplace pressure is given by $p = -\sigma \Delta \rho + V'(\rho)$ and the surface tension $\sigma \approx 30.8 \text{ mN m}^{-1}$. The non-negative mobility coefficient $m(\rho)$ vanishes for $\rho = 0$ and depends on the boundary conditions of the liquid flow at the substrate—e.g. no-slip entails $m(\rho) = \rho^3/3$.

In [1] Minkowski functionals are used for a quantitative analysis of the evolution of dewetting patterns. Simulated dewetting morphologies (figure 13(a), bottom) based on equation (34) are gained by using the identical experimental system parameters of a dewetting polymer film, which was analyzed *in situ* by atomic force microscopy (figure 13(a), top) and other techniques to determine film morphology, film thickness, viscosity and surface tension. In figure 13(a) the film surface develops a correlated pattern of indentations and finally ruptures. Numerical solutions of equation (34) and experimental data are in close agreement which can already be seen by looking at the timescales involved. The quantitative comparison of simulations and experiments is enabled by pattern analysis based on integral geometry which provides accurate comparison tools beyond visual inspection [5]. This is of particular relevance as the morphology of the rupturing film has two contributions of different character: while the holes are easy to identify by eye, a description of the film in between the holes requires

a closer inspection. For this we introduce isosurfaces $\rho(\vec{x}, t) = l$, where ρ is a fixed threshold value. Then, the Minkowski functionals, the area $F(\rho)$, boundary length $U(\rho)$ and Euler characteristic $\chi(\rho)$ are determined in order to characterize the resulting set of black and white images. These functions are sensitive to the geometry of the film surface and measure spatial features which cannot be captured by other means, e.g. a Fourier transform. Surprisingly, this morphometric analysis shows that experiments and simulations shown in figure 13(a) follow both a Gaussian random field model for contours above the average film thickness $\rho_0 \approx 0$, namely a constant $s(\rho) = -F'(\rho)/U(\rho) = s_0$, a parabolic $u(\rho) = \log U(\rho) = u_2(\rho - \rho_0)^2$ and a linear behaviour in the curvature $\kappa(\rho) = \kappa_1(\rho - \rho_0)$ (compare equation (27)).

In figure 13(b) the time-averaged normalized data for $s(\rho)$, $u(\rho)$ and $\kappa(\rho)$ are shown and a good agreement between model expectation and data are found for each snapshot at any given time. Only the parameters $s_0 = t^{-\nu_s}$, $u_2 = t^{-\nu_u}$ and $\kappa_1 = t^{-\nu_\kappa}$ depend on time t over at least two decades. An excellent consistency check is again provided by equation (28), i.e. by the ratios $X = e^{-2u_0} s_0 / \kappa_1 \approx 1.57$ and $Y = s_0 \kappa_1 / u_2 \approx 0.203$ (figure 13(c)) which nevertheless remains constant for Gaussian random fields (solid line). Moreover, the expected zeros $u(\rho_0) \approx 0$ and $\kappa(\rho_0) \approx 0$ are matched by experiments and simulations for all times. Of course, the results can depend slightly on the averaging procedure as well as on the algorithm for $m_\nu(\rho)$ and the fitting procedure to obtain X and Y . But we find only small differences when comparing the improved results presented here with the previous data shown in [1]. It is interesting to note that, in the simulations, the stadium until first holes are generated is reached much later than in the experiments. A detailed study focusing on the timescale revealed that thermal fluctuations help in the experiments to speed up the initial stadium [33]. Thus, the deterministic Navier–Stokes equation given by equation (34) in a lubrication approximation has to be extended by a stochastic noise term to match the experimental data [34].

Our morphometric image analysis with Minkowski functionals demonstrates the capability of the thin film model to quantitatively describe the dynamical evolution of thin film rupture. The development of the film profiles for different complex evolution patterns can thus be monitored in both space and time. Our pattern analysis approach reveals that the spinodally dewetting liquid film evolves as a correlated Gaussian random field with a time-dependent variance. As a consequence of the good quantitative agreement of the theoretical model, experiment and simulation of thin film rupture over a time interval exceeding the initial rupture event by far, the full dynamical evolution of complex film patterns becomes accessible, having impact on many advances in thin film technologies at nanometre scales.

6. Conclusion

Measuring the shape of curved objects in images is a common challenge in image analysis and physics. The shape of disordered structures is a remarkably incoherent concept and cannot be captured by correlation functions alone which were almost a synonym for structural analysis in statistical physics since the very first x-ray scattering experiments. However, in the last 20 years numerous methods such as scanning force microscopy and computed x-ray tomography have been developed which allow quantitative measurements of complex structures directly in real space. Integral geometry furnishes a suitable

family of morphological descriptors, known as Minkowski functionals, which are related to curvature integrals and do not only characterize connectivity (topology) but also size and shape of disordered structures.

Here, we have demonstrated a way to tackle the problem for digitized grey-scale images that are made up by pixels. The clue is to refine the contours of the pixelized objects. Therefore, the pixels have to be subdivided and replaced by polygons, the form of which is determined by the information provided by the grey-scale of neighbouring pixels and by the threshold that has been set. This method of weighted side lengths in a marching square algorithm is a very powerful tool to numerically determine Minkowski functionals for irregular objects. For the analysis of 3D data consisting of voxels, a similar algorithm can be used; the marching cube algorithm, for example, for rendering 3D medical images gained by computed x-ray tomography or for characterization of porous media [7, 25, 26].

The given examples for the characterization and analysis of morphologies range from dewetting films to pattern formation in chemical reactions and demonstrate the applicability of the method. The Minkowski functionals of the morphology as a function of threshold thereby serve as a ‘fingerprint’ that can be compared with other morphologies. For dewetting films we have exemplarily shown the comparison of an experimental and a simulated series of pictures. As additional material we provide the implementation of the algorithm in C and in Java with a platform-independent graphical user interface. It can be used for many practical applications, e.g. for the quality control of surfaces or for the characterization of foamy or other multi-component materials, to name just a few.

References

- [1] Becker J, Grün G, Seemann R, Mantz H, Jacobs K, Mecke K and Blossey R, *Complex dewetting scenarios captured by thin film models*, 2003 *Nat. Mater.* **2** 59
- [2] Cressie N A C, 1991 *Statistics for Spatial Data* (New York: Wiley)
- [3] Lohmann G, 1998 *Volumetric Image Analysis* (New York: Wiley) (Leipzig: Teubner)
- [4] Torquato S, 2002 *Random Heterogeneous Materials* (New York: Springer)
- [5] Mecke K and Stoyan D, 2000 *Statistical Physics and Spatial Statistics: The Art of Analyzing and Modeling Spatial Structures and Pattern Formation* (Springer Lecture Notes in Physics vol 554) (Heidelberg: Springer)
- [6] Mecke K and Stoyan D, 2002 *Morphology of Condensed Matter-Physics and Geometry of Spatially Complex Systems* (Springer Lecture Notes in Physics vol 600) (Heidelberg: Springer)
- [7] Arns C H, Knackstedt M A and Mecke K, *Reconstructing complex materials via effective grain shapes*, 2003 *Phys. Rev. Lett.* **91** 215506
- [8] Aarts D G A L and Lekkerkerker H N W, *Confocal scanning laser microscopy on fluid–fluid demixing colloid–polymer mixtures*, 2004 *J. Phys.: Condens. Matter* **16** S4231
- [9] Aarts D G A L, Dullens R P A and Lekkerkerker H N W, *Interfacial dynamics in demixing systems with ultralow interfacial tension*, 2005 *New J. Phys.* **7** 40
- [10] Mecke K, *Morphological characterization of patterns in reaction–diffusion systems*, 1996 *Phys. Rev. E* **53** 4794
- [11] Rosenfeld A and Kak A C, 1982 *Digital Picture Processing* (New York: Academic)
- [12] Serra J, 1982 *Image Analysis and Mathematical Morphology vol 1: Theoretical Advances* (London: Academic)
- [13] Ohser J and Mücklich F, 2000 *Statistical Analysis of Microstructures in Materials Science* (Chichester: Wiley)
- [14] Mecke K, *Integralgeometrie in der statistischen physik*, 1993 *PhD Thesis* Ludwig-Maximilians-Universität München
- [15] Mecke K, *Integral geometry in statistical physics*, 1998 *Int. J. Mod. Phys. B* **12** 861
- [16] Hadwiger H, 1957 *Vorlesungen über Inhalt, Oberfläche und Isoperimetrie* (Berlin: Springer)
- [17] Lindemann F, *Über die Zahl π* , 1882 *Math. Ann.* **20** 213

- [18] Lorensen W and Cline H, *Marching cubes: a high resolution 3d surface construction algorithm*, 1987 *Proc. SIGGRAPH'87 (Anaheim, CA, Juli 1987)*; *Comput. Graph.* **21** 163
- [19] Tomita H, *Statistics and geometry of random interface systems*, 1990 *Formation, Dynamics and Statistics of Patterns* vol 1, ed K Kawasaki, M Suzuki and A Onuki (Singapore: World Scientific) pp 113–57
- [20] Kerscher M, Mecke K, Schmalzing J, Beisbart C, Buchert T and Wagner H, *Morphological fluctuations of large-scale structure: the pscz survey*, 2001 *Astron. Astrophys.* **373** 1
- [21] Kerscher M, Mecke K, Schuecker P, Bohringer H, Guzzo L, Collins C A, Schindler S, De Grandi S and Cruddace R, *Non-Gaussian morphology on large scales: Minkowski functionals of the REFLEX cluster catalogue*, 2001 *Astron. Astrophys.* **377** 1
- [22] Stoyan D and Mecke K, *The boolean model: from matheron till today*, 2005 *Space, Structure and Randomness, Contributions in Honor of Georges Matheron in the Fields of Geostatistics, Random Sets, and Mathematical Morphology (Springer Lecture Notes in Statistics vol 183)* ed M Bilodeau, F Meyer and M Schmitt (New York: Springer) pp 151–82
- [23] Mecke K and Wagner H, *Euler characteristic and related measures for random geometric sets*, 1991 *J. Stat. Phys.* **64** 843
- [24] Mecke K, Buchert T and Wagner H, *Reconstructing complex materials via effective grain shapes*, 1994 *Astron. Astrophys.* **288** 697
- [25] Arns C H, Knackstedt M A, Pinczewski W and Mecke K, *Euler-Poincaré characteristics of classes of disordered media*, 2001 *Phys. Rev. E* **63** 31112
- [26] Arns C H, Knackstedt M A and Mecke K, *Characterisation of irregular spatial structures by parallel sets and integral geometric measures*, 2004 *Colloids Surf. A* **241** 351
- [27] König P M, Roth R and Mecke K, *Morphological thermodynamics of fluids: shape dependence of free energies*, 2004 *Phys. Rev. Lett.* **93** 160601
- [28] Rehse S, Mecke K and Magerle R, *Characterization of the dynamics of block copolymer microdomains with local morphological measures*, 2008 *Phys. Rev. E* **77** 051805
- [29] Knüfing L, Schollmeyer H, Riegler H and Mecke K, *Fractal analysis methods for solid alkane monolayer domains at SiO₂/Air interfaces*, 2005 *Langmuir* **21** 992
- [30] Mecke K and Stoyan D, *Morphological characterization of point patterns*, 2005 *Biometrical J.* **47** 473
- [31] Ouyang Q and Swinney H L, *Transition to chemical turbulence*, 1991 *Chaos: Interdiscip. J. Nonlinear Sci.* **1** 411
- [32] Seemann R, Herminghaus S and Jacobs K, *Dewetting patterns and molecular forces: a reconciliation*, 2001 *Phys. Rev. Lett.* **86** 5534
- [33] Fetzer R, Rauscher M, Seemann R, Jacobs K and Mecke K, *Thermal noise influences fluid flow in thin films during spinodal dewetting*, 2007 *Phys. Rev. Lett.* **99** 114503
- [34] Mecke K and Rauscher M, *On thermal fluctuations in thin film flow*, 2005 *J. Phys.: Condens. Matter* **17** S3515